RSC Advances

PAPER

View Article Online
View Journal | View Issue

Cite this: *RSC Adv.*, 2022, **12**, 1728

Urchin-like hollow SiO_2@γ-MnO_2 microparticles for the rapid degradation of organic dyes†

Zhuo-Rui Li,‡ Xiao-Hui Zhang,‡ Yue-Yue Du and Guo-Zhi Han *

In this paper, using hollow silica microspheres as carriers, we developed a facile one-pot method for the preparation of hollow SiO_2@MnO_2 composite microparticles. Under a certain proportion of hollow silica microspheres and manganese salt, a novel kind of hollow urchin-like SiO_2@γ-MnO_2 microparticles was obtained. The structure and morphology of the composite microparticles were characterized by XRD, SEM and TEM. On this basis, using rhodamine B and methyl orange as model molecules, the oxidative degradation ability of the hollow SiO_2@γ-MnO_2 microparticles for organic dyes in water was investigated through UV-vis analysis technology. The urchin-like SiO_2@γ-MnO_2 microparticles showed excellent performance for the rapid oxidative degradation of organic dyes under acidic conditions. This study indicated that γ-MnO_2 loaded on hollow materials can be used as an efficient tool for treating organic dye wastewater, and shows broad application prospects for solving environmental problems in the related industry.

Received 28th August 2021
Accepted 13th December 2021

DOI: 10.1039/d1ra06490h

rsc.li/rsc-advances

1. Introduction

Organic dyes are mostly aromatic heterocyclic compounds with stable molecule structures and chromogenic groups, which can cause great harm if leaked into the environment. In past decades, printing and dyeing wastewater has always been an important problem for industrial water treatment. According to statistics, the current discharge accounts for 35% of total industrial wastewater, and contains a large number of complex components such as dyes, pulp, surfactants, and alkali agents.[1–6] Generally, the removal of organic pollutants in dye wastewater can be divided into physical methods and oxidation methods. However, the physical methods do not destroy the organic pollutant molecules themselves, which needs further follow-up treatment and may cause secondary pollution. Therefore, chemical methods have become the main research hotspots for printing and dyeing wastewater treatment.[7,8] Among them, advanced oxidation processes (AOPs) are a very effective technology for the treatment of refractory organic compounds. Their essence is that free radicals degrade various organic pollutants in wastewater by means of electron transfer, as well as addition and dehydrogenation reactions into CO_2, H_2O and other harmless substances.[9]

AOPs mainly include wet oxidation, photocatalytic oxidation, and electrochemical oxidation. They can convert many organic compounds with stable structures that are also difficult to biodegrade into non-toxic, harmless and biodegradable low molecular weight substances. This characteristic endows AOPs with broad application prospects in the advanced treatment of printing and dyeing wastewater.[10–12] Among AOPs, the oxidative degradation of organic pollutants by transition metal oxides has attracted extensive attention due to its high efficiency and low cost.[13–19] In particular, manganese oxide (MnO_2) has become a widely-used agent for treating different kinds of organic dyes because of its high stability, good environmental compatibility, and variable valence.[20–23] On the other hand, for oxidative degradation, the degradation efficiency of organic pollutants largely depends on the degree of the pollutants close to the surface of active metal oxides. However, MnO_2 particles prepared by traditional methods such as the hydrothermal method and coprecipitation have low specific surface areas, which seriously reduces their actual efficiency in the treatment of organic pollutants in water. To solve this problem, many research efforts have been devoted to constructing various types of MnO_2 microparticles with high specific surface area.[24–30] In fact, MnO_2 microparticles have variable crystal forms and structures due to different [MnO_6] octahedral unit links, and the common crystal forms include α-MnO_2, γ-MnO_2, β-MnO_2 and δ-MnO_2.[31] Among them, the octahedral units in γ-MnO_2 form multi-chains along the *c*-axis, eventually resulting in two-dimensional infinite lamellae with large specific surface area, abundant adsorption sites, and high chemical activity. Meanwhile, γ-MnO_2 mainly exists in the form of hydrate and has a large number of hydroxyl groups on its surface, which is beneficial for the enrichment of organic dyes on its surface. In recent years, the research on γ-MnO_2 for AOPs has stimulated

College of Chemistry and Molecular Engineering, Nanjing Tech University, Nanjing, 211816, P. R. China. E-mail: han@njtech.edu.cn

† Electronic supplementary information (ESI) available. See DOI: 10.1039/d1ra06490h

‡ The two authors contributed equally to this work.

an extensive interest in the field of treatment of organic dyes in wastewater.[32–36] In addition, it is well known that materials with excellent performance depend not only on the crystalline structure and composition but also on the morphology; sometimes, even the influence of morphology plays a key role in the physicochemical performance.[37,38] To date, MnO_2 microparticles with different morphology, including 0-D nanoparticles, 1-D nanowires, nanorods, nanotubes, 2-D nanosheets, as well as 3-D hierarchical nanostructures, have been successfully prepared. In the above-mentioned microstructures, the 3-D hierarchical nanostructures such as flower-like microparticles have attracted great attention due to their higher specific surface area, more active sites, and low densities along with better penetration.[39–42] However, the synthesis of 3-D hierarchical MnO_2 microstructures requires complex steps, which leads to a low synthesis efficiency.[36] Herein, based on our previous studies,[43] using hollow silica microspheres as the carrier, we developed a facile method to prepare a kind of novel urchin-like hollow SiO_2@γ-MnO_2 microparticles by the one-pot redox precipitation method, as shown in Fig. 1. Furthermore, using rhodamine B and methyl orange as the models, we studied the oxidative degradation ability of the composite microparticles for the organic dyes in water. The research results indicate that the as-prepared urchin-like hollow SiO_2@γ-MnO_2 microparticles show excellent oxidation degradation performance for organic dyes. Under acidic conditions, organic dyes in water can be completely degraded in about 30 min. This work illustrates that γ-MnO_2 microparticles loaded on hollow materials can be used as an efficient tool to treat organic pollutants in water, and show broad application prospects for solving some important environmental problems in the related industry.

2. Experimental section

2.1 Materials and instruments

Styrene (St), α-methacrylic acid (MAA), potassium permanganate ($KMnO_4$), hydrochloric acid (HCl), and sodium hydroxide (NaOH) were purchased from Shanghai Lingfeng Chemical Reagent Co., Ltd. Manganese nitrate tetrahydrate ($MnN_2O_6 \cdot 4H_2O$) and tetraethyl orthosilicate (TEOS) were purchased from Aladdin Industrial Corporation (Shanghai, China). Anhydrous ethanol (EtOH) was purchased from Wuxi City Yasheng Chemical Reagent Co., Ltd. Potassium persulfate ($K_2S_2O_8$), ammonia (NH_3 H_2O), and rhodamine B (RhB, $C_{28}H_{31}ClN_2O_3$) and methylene blue ($C_{16}H_{18}ClN_3S$) were purchased from Sinopharm Chemical Reagent Co., Ltd. Polyvinylpyrrolidone ($(C_6H_9NO)_n$) and methyl orange ($C_{14}H_{14}N_3SO_3Na$) were purchased from Shanghai Yuanye Bio-Technology Co., Ltd. All chemical reagents were of analytical grade and used without any further purification. Deionized water was obtained from Wahaha Group Co., Ltd and used in all experiments.

The UV-vis spectra were recorded on a UV-3600 spectrophotometer (Shimadzu, Japan). Scanning electron microscopy (SEM) images were obtained by a Jeiss Ultra Plus SEM microscope (Carl Zeiss, Germany). The TEM observations in this paper were performed on a JEM-2100 transmission electron microscope (JEOL Japan). X-ray diffraction (XRD) patterns were recorded on a D8 ADVANCE X-ray diffractometer (Bruker, Germany) with Ni-filtered CuKα radiation (40 kV, 40 mA). The high temperature calcination of the as-prepared materials was carried out in a GSL-1100X tubular furnace (HF Kejing, China). In this paper, all tests of the same type were performed under the same conditions.

2.2 Synthesis of hollow SiO_2 microspheres by the template method

Firstly, 250 mL ultrapure water, 8 mL (0.069 mol) styrene, 0.16 g (0.6 mmol) potassium persulfate, and 0.32 mL (3.2 mmol) α-methacrylic acid were successively added into a 500 mL three-neck flask equipped with a condensation tube, followed by heating to 75 °C under the protection of argon. After stirring uniformly for 12 h, carboxylated polystyrene microspheres (PS) were obtained by centrifugation and washing with water several times. Secondly, 0.26 g (7.2×10^{-4} mmol) polyvinylpyrrolidone (PVP) and 40 mL ultrapure water were added into a 250 mL single-neck flask. After ultrasonic treatment for 1 h, the mixture completely formed a colorless solution. Subsequently, 1 g of the as-prepared PS microspheres and 40 mL anhydrous ethanol were added into the solution. After stirring at a constant speed for 24 h, PVP-modified carboxylated PS microspheres were obtained, which acted as the template for the synthesis of hollow SiO_2 microspheres.

The hollow SiO_2 microspheres were synthesized by the template method described as follows. The as-prepared PVP-modified PS microspheres were mixed with 73.5 mL

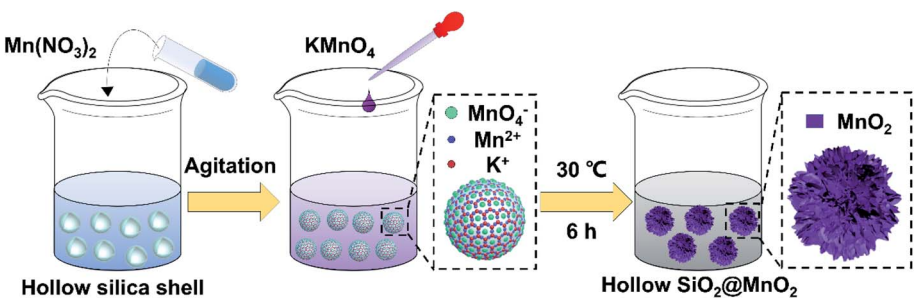

Fig. 1 The synthetic route of the urchin-like hollow MnO_2 microparticles.

anhydrous ethanol and 3.87 mL ammonia (25 wt%) in a 250 mL single-neck flask under stirring. Then, 0.08 mL, 0.08 mL, 0.16 mL, and 0.32 mL of tetraethyl orthosilicate (10 vol% in absolute ethanol) were successively dropped into the solution at the rate of 0.04 mL min^{-1} with an interval of two h. After stirring for 12 h at room temperature, the core–shell PS@SiO_2 microparticles were obtained by centrifugation. Finally, the hollow silica shells were prepared by calcining the PS@SiO_2 microparticles at 700 °C for 6 h in air atmosphere.

2.3 Preparation of urchin-like hollow SiO_2@γ-MnO_2 microparticles

The urchin-like hollow SiO_2@γ-MnO_2 microparticles were prepared by the one-pot redox precipitation method, which is described as follows. Firstly, 0.02 g hollow silica microspheres, 0.173 g (0.689 mmol) manganese nitrate tetrahydrate and 20 mL ultrapure water were added into a 50 mL single-neck flask, followed by ultrasonication for 1 h. Then, 0.073 g (0.462 mmol) $KMnO_4$ was added into 10 mL ultrapure water to form a homogeneous solution, which was subsequently dropped into the above mixture solution at the rate of 0.5 mL min^{-1} under stirring. Subsequently, the color of the mixture solution changed from white to light brown, and finally to purple brown. The resulting solution was then stood at 30 °C for 6 h until the solution color turned black. Finally, after centrifuging and washing with water several times, the black urchin-like hollow SiO_2@MnO_2 microparticles were obtained by drying at 80 °C overnight. On this basis, parallel experiments were carried out with different amounts of hollow silica microspheres to study the effect of the reaction materials' ratio on the morphology of the products.

2.4 Degradation of organic dyes by the hollow SiO_2@γ-MnO_2 microparticles

In the oxidative degradation process, rhodamine B (RhB) was first selected as the dye model molecule. The specific operation steps are shown as follows. First, 5 mL rhodamine B (RhB) aqueous solution (0.05 mmol L^{-1}) was added to 25 mL ultrapure water, and 0.1 M HCl or NaOH solution was used to adjust the pH value of the initial solution. Then, the quantitative as-prepared SiO_2@γ-MnO_2 microparticles were added into the above solution under magnetic stirring. At a given time interval, the oxidative degradation process was monitored by UV-Vis spectrophotometry. The oxidation degradation rate of RhB was investigated by the following formula.

$$б = \frac{A_0 - A_t}{A_0} \times 100\% \quad (1)$$

where A_0 is the initial concentration of RhB and A_t is the concentration of RhB at a certain time interval. The concentration of RhB is determined by its peak intensity at the maximum absorption. In order to optimize the experimental conditions, the effects of oxidants with different morphologies and pH values (2, 3.5, 5, 7, 10.5) on the degradation efficiency were investigated.

3. Results and discussion

3.1 Characterization of the hollow SiO_2@γ-MnO_2 microparticles

In this paper, using hollow silica microspheres as the framework, the hollow SiO_2@γ-MnO_2 microparticles were synthesized by a controlled redox precipitation method under low temperature, as shown in the following formula (2).

$$2KMnO_4 + 3Mn(NO_3)_2 + 2H_2O \rightarrow 5MnO_2 + 4HNO_3 + 2KNO_3 \quad (2)$$

In the reaction, the MnO_2 layer is formed on the surface of SiO_2 by the reactive deposition of the manganese precursor. There is no doubt that the ratio of hollow SiO_2 microspheres to manganese salt has a great influence on the morphology of the final product. Therefore, we conducted a series of parallel synthetic experiments with different amount ratio of hollow SiO_2 microspheres to the manganese precursor. Table 1 shows the raw material parameters of the parallel experiments.

Fig. 2 shows the corresponding SEM and TEM images of the products prepared under different conditions. The experimental results indicate that, with the change in the amount ratio of the raw materials, the morphologies of the synthesized products changed greatly. When the amount of hollow SiO_2 microspheres was relatively large, the deposited MnO_2 cannot completely cover the surface of the hollow SiO_2 microspheres, forming an uneven and discontinuous microsphere appearance. With the decrease in the amount of the SiO_2 microspheres, the surface of hollow SiO_2 microspheres was gradually coated by MnO_2. Under a certain proportion, a kind of urchin-like hollow MnO_2 microparticles with radial spinous surface were obtained, as shown in Fig. 2(C and H). When the amount of hollow SiO_2 microspheres is too small, it will cause the collapse of the sheet structure of MnO_2 and form the black MnO_2 particles.

Fig. 3 shows the EDS-mapping of the urchin-like hollow SiO_2@γ-MnO_2 microparticles and the control sample. It is observed that the element ration of Mn/Si on the surface of the urchin-like hollow SiO_2@γ-MnO_2 microparticles is much higher than that of the reference sample, *i.e.*, on the surface of the urchin-like hollow SiO_2@γ-MnO_2 microparticles, MnO_2 is more evenly distributed on the surface of the SiO_2 carrier, which is also consistent with the observation by the electron microscope. Based on the acidic state in the preparation process, we speculate that under the condition of a certain amount of carrier, more uniform protonation sites can be formed on the

Table 1 Raw material parameters of the parallel experiments

Hollow-SiO_2	$MnN_2O_6 \cdot 4H_2O$	$KMnO_4$
0.08 g	0.173 g	0.073 g
0.04 g	0.173 g	0.073 g
0.02 g	0.173 g	0.073 g
0.005 g	0.173 g	0.073 g
0	0.173 g	0.073 g

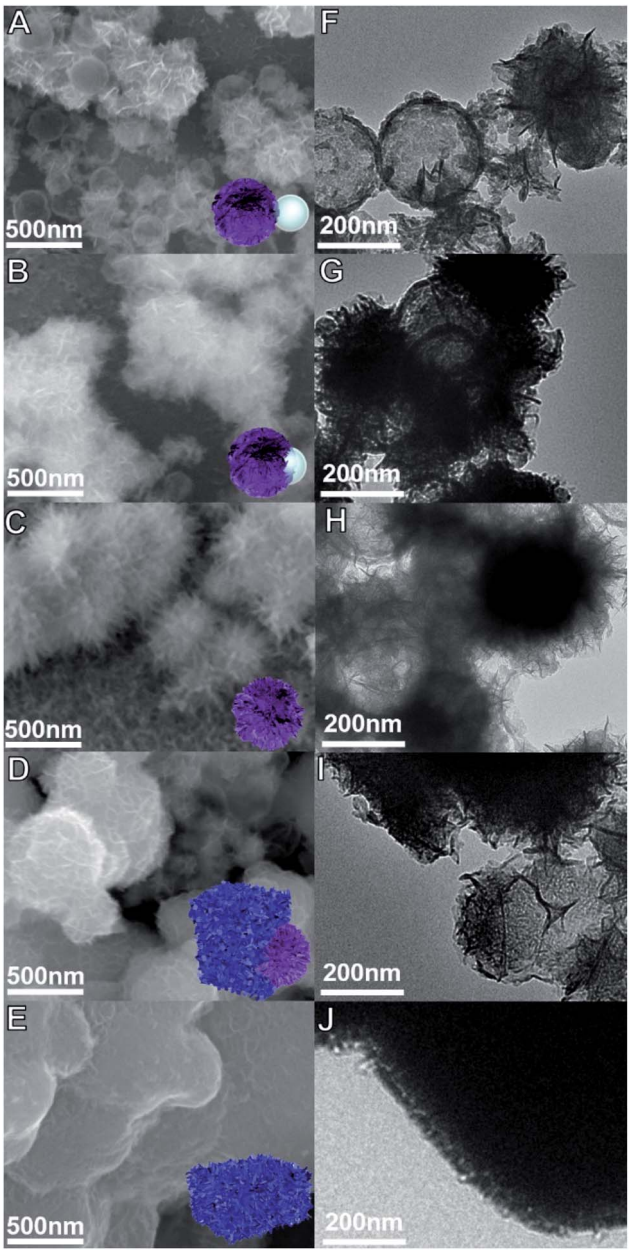

Fig. 2 The SEM and corresponding TEM images of SiO_2@γ-MnO_2 microparticles prepared under different conditions. (Amount of hollow SiO_2 microspheres: A, F: 0.08 g, B, G: 0.04 g, C, H: 0.02 g, D, I: 0.005 g, E, J: 0).

surface of hollow SiO_2 microspheres, which is conducive for the aggregation of manganese nitrate and the formation of a uniform reaction center. After the addition of potassium permanganate, the crystal grows longitudinally due to the electrical exclusion of the MnO_2 nanocrystal surface, and finally forms the urchin-like structure. According to the above reasoning, the increase or decrease of hollow SiO_2 microspheres is not conducive for the formation of the urchin-like structure.

The crystal structure of the urchin-like hollow SiO_2@γ-MnO_2 microparticles was determined by X-ray diffraction, as shown in Fig. 4. The peaks at 23.4°, 37.2°, 42.5°, 57°, and 65.7° can be assigned to the lattice planes of (1 2 0), (1 3 1), (3 0 0), (1 6 0), and (4 2 1) in hexagonal type MnO_2, respectively (γ-MnO_2, JCPDS 14-0644 crystal system: orthorhombic, lattice parameters: 6.36 × 10.15 × 4.09 Å). The wide peak near 22° proves the existence of the silica shell skeleton. Generally, a higher concentration of manganese ion is beneficial for the formation of the γ-MnO_2 phase at low temperature.[44,45] This theory is consistent with our synthetic strategy that potassium permanganate was added to the suspension containing divalent manganese ions. Though the γ-MnO_2 phase is metastable and can be transformed into the α-MnO_2 phase. However, the previous reports shows that the γ-MnO_2 phase can be stabilized at a lower reaction temperature (≤60 °C) and shorter reaction time of the MnO_4^-/Mn^{2+} system. At the same time, our work shows that the tunnel structures of γ-MnO_2 can be easily obtained by simple control in the process of precursor addition.[46]

3.2 Degradation activity of the hollow urchin-like SiO_2@γ-MnO_2 microparticles for dyes

The degradation of dye in water by MnO_2 is realized by the oxidative reaction. The redox reaction can be expressed as $MnO_2(s) + 4H^+ + 2e^- \rightarrow Mn^{2+}(aq) + 2H_2O$. Therefore, a low pH value can improve the reducing potential of MnO_2/Mn^{2+} as well as the oxidizing power of the system, which means that low pH is in favor of the oxidative degradation of the dyes.[47] Fig. 5 shows the UV-Vis spectra of rhodamine B solution at different pH values (2, 3.5, 5, 7, 10.5) in the presence of urchin-like hollow γ-MnO_2 microparticles (1.5 mg mL^{-1}) and in the absence of the catalyst. The experimental results indicated that the characteristic peak of rhodamine B decreased significantly, and the maximum peak blue shifted under acidic conditions, *i.e.*, the degradation rate of RhB under acidic conditions was higher than that under alkaline conditions. In this process, the color of the solution began to gradually change from pink to colorless and transparent. When the pH value of solution > 7, the UV-Vis spectra of the rhodamine B solution hardly changed within 24 h. The parallel blank experiment showed that the RhB solution had only slight natural degradation in the absence of MnO_2 under acidic conditions. Moreover, there is no doubt that the attenuation of characteristic peaks of RhB is not caused by adsorption because adsorption rarely leads to a blue shift of the absorption peak. On the other hand, under acidic conditions, the surface of MnO_2 is prone to protonation and subsequent positive charge, which is not conducive to the adsorption of RhB. If the fading of the dyes originates from the pure adsorption of RhB on the SiO_2@γ-MnO_2 microparticles, it would be enhanced with the increase in the solution pH, which is contrary to our experimental results. Therefore, the degradation of RhB is not caused by adsorption.

Fig. 6(A) shows the corresponding degradation curve of RhB under different pH conditions. Within 10 min, the degradation rates of RhB at pH = 2, 3.5, and 5 were 90.6%, 87.1%, and 71.6%, respectively. However, in the case of pH = 7, the degradation rate of RhB was only 54.4% within 10 min and there was almost no change after 24 h. This phenomenon may be due to that the small molecular amines produced in the

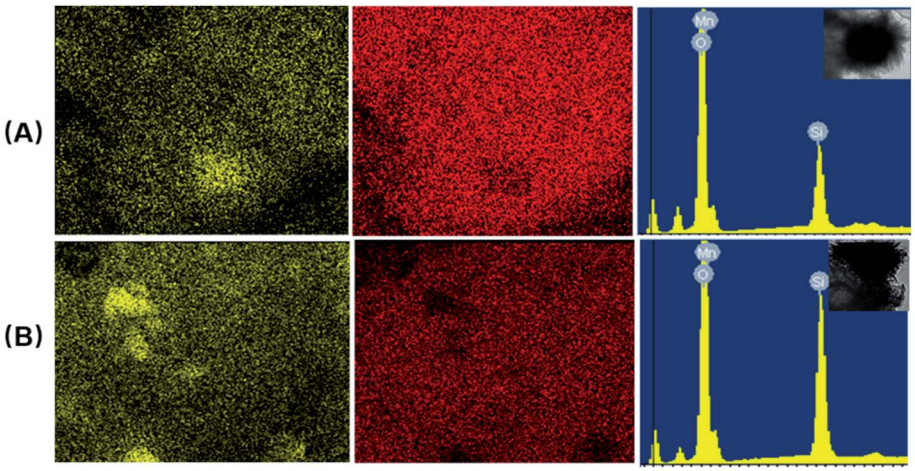

Fig. 3 EDS-mapping of the urchin-like hollow SiO_2@γ-MnO_2 microparticles ((A): 0.02 g hollow SiO_2 microspheres) and the control sample ((B): 0.04 g hollow SiO_2 microspheres).

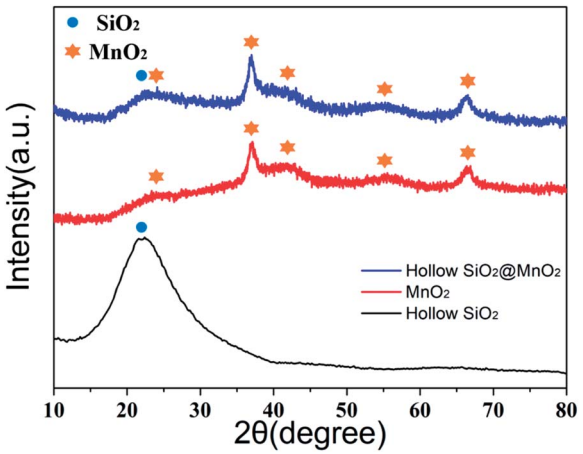

Fig. 4 XRD patterns of the urchin-like hollow SiO_2@γ-MnO_2 microparticles, hollow-SiO_2 shell and pure MnO_2 particles.

degradation process, which decreased the oxidation ability of MnO_2. However, the degradation rate of rhodamine was almost zero in 24 h at pH = 10.5. According to the experimental results, the degradation kinetics curve was drawn with $\ln(A_0/A_t)$ as the ordinate and time t as the abscissa, as shown in Fig. 6(B). It can be seen from the results that there is a good linear relationship between $\ln(A_0/A_T)$ and T at different pH, which indicates that the oxidative degradation of RhB by the urchin-like SiO_2@γ-MnO_2 microparticles under different pH conditions conforms to the characteristics of quasi first-order kinetics. Therefore, the degradation of the organic dye by the urchin-like SiO_2@γ-MnO_2 microparticles can be described by the L–H kinetic model, and the migration of the dye to the microparticle surface follows the state of monolayer adsorption.

In order to investigate the effect of material morphology on the oxidative degradation ability, rhodamine B was further degraded by the different as-prepared SiO_2@MnO_2 microparticles under acidic conditions (pH = 3.5). The experimental results indicated that the urchin-like SiO_2@MnO_2 microparticles show better degradation ability, as shown in Fig. 7. Under the catalysis of the urchin-like hollow SiO_2@γ-MnO_2 microparticles, RhB was basically degraded completely within 30 min, whereas the absorption peak of the RhB solution decreased only about 50% under the catalysis of the other three kinds of materials. As for catalysis by pure MnO_2 particles, the absorption peak of the RhB solution decreased about 61%, as shown in Fig. S1.† In addition, pure hollow silica microspheres have no catalytic effect. It is exciting that compared with other materials, the urchin-like SiO_2@MnO_2 microparticles show ultra-high activity in the degradation of rhodamine B. Except the urchin-like SiO_2@MnO_2 microparticles, it takes 4–24 h for other materials to reach a high degradation rate of RhB. This phenomenon may be attributed to the fact that the urchin-like structure has better active sites and specific surface area.

In order to investigate the general adaptation of the urchin-like SiO_2@γ-MnO_2 microparticles for dye degradation applications, we further studied the degradation of methylene blue and methyl orange by the urchin-like SiO_2@γ-MnO_2, as shown in Fig. 8. The experimental results show that the as-prepared urchin-like SiO_2@γ-MnO_2 still have good degradation performance for the two dyes, and the degradation rate of methylene blue and methyl orange can reach 83.6% and 87.5% in 10 min, respectively. Our studies indicate that the as-prepared urchin-like SiO_2@γ-MnO_2 microparticles have strong oxidative degradation ability for organic dyes with different charge characteristics.

In practice, printing and dyeing wastewater may contain a variety of dyes. In order to study the effect of a mixed system on the degradation performance of the urchin-like hollow SiO_2@γ-MnO_2 microparticles, we next studied the degradation performance of the materials for simulated mixed dye wastewater. Fig. 9 shows the UV-Vis spectra of the mixed solution containing two dyes with different charge characteristics in the presence of urchin-like hollow γ-MnO_2 microparticles. The experimental results show that the synthesized urchin-like hollow γ-MnO_2 microparticles still show good degradation

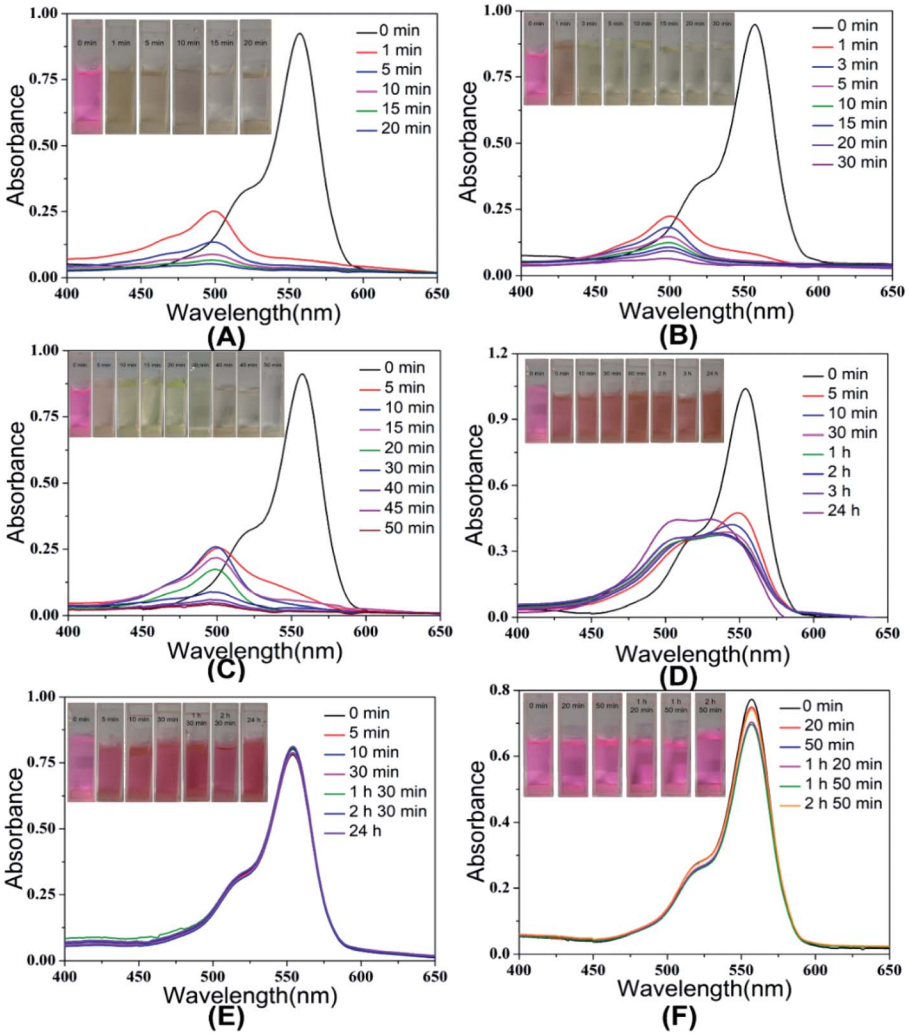

Fig. 5 UV-Vis spectra of RhB degradation by the urchin-like hollow SiO_2@γ-MnO_2 microparticles at different pH ((A): pH = 2, (B): pH = 3.5, (C): pH = 5, (D): pH = 7, (E): pH = 10.5, (F): pH = 3.5 without catalyst).

performance for the mixed dye system. However, it shows better degradation behavior for mixed dyes with different charge characteristics. For the mixed solution of the anionic dye of methyl orange and the cationic dye of methylene blue, it basically fades after 20 min, whereas for the mixed solution of the

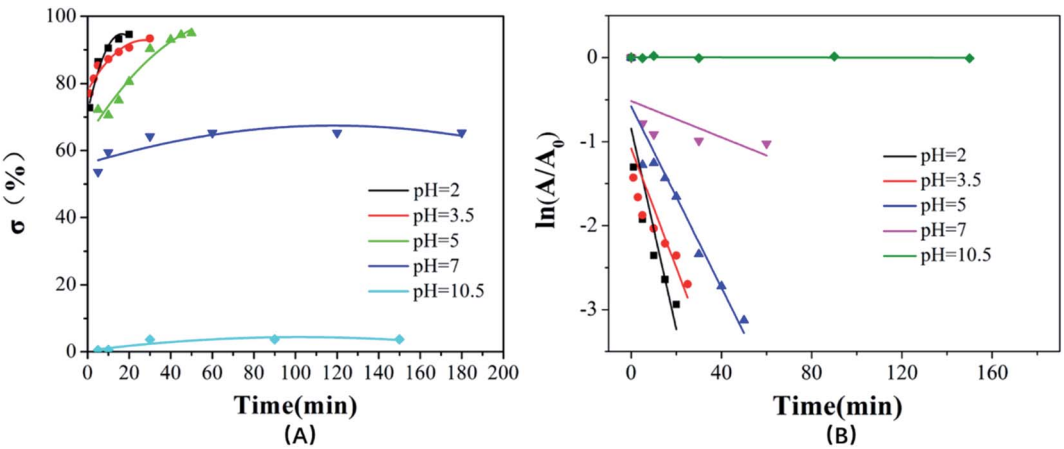

Fig. 6 The degradation curve (A) and kinetic curves (B) of RhB by the urchin-like SiO_2@γ-MnO_2 microparticles at different pH.

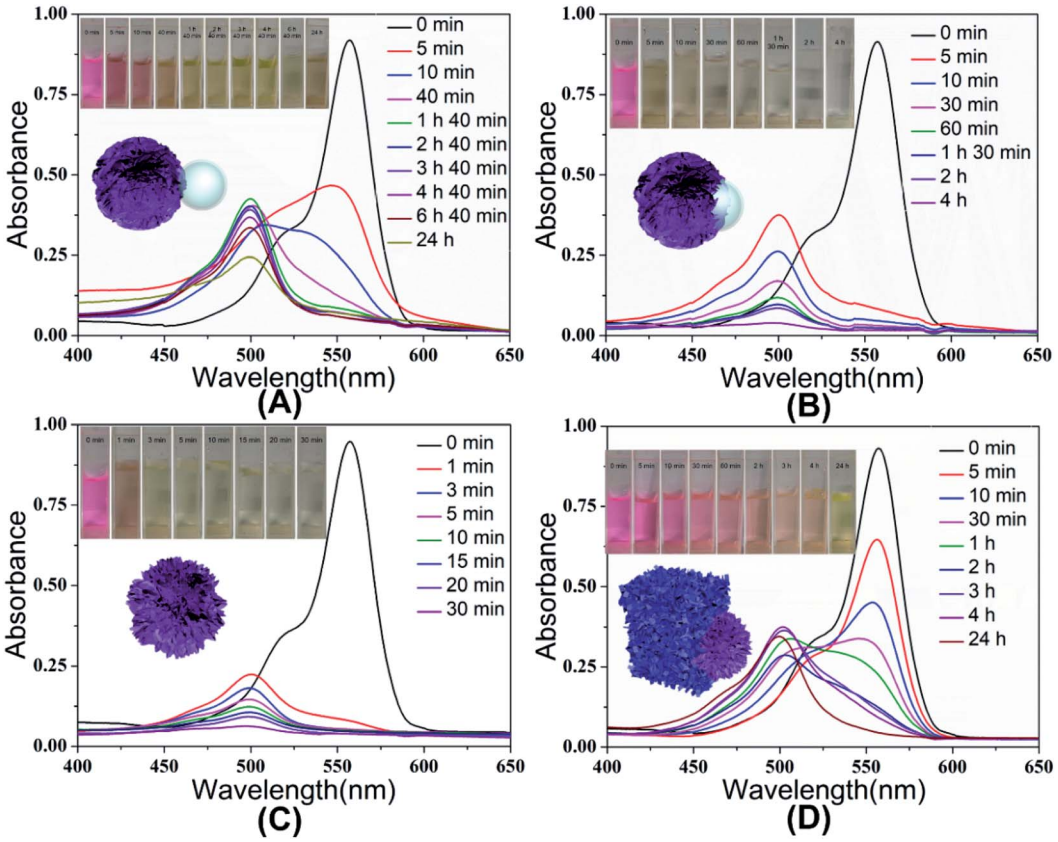

Fig. 7 UV-Vis spectra of RhB solution with the existence of different as-prepared SiO_2@γ-MnO_2 microparticles at pH = 3.5.

cationic dye of rhodamine B and methylene blue, the degradation rate is about 80% after 35 min.

Fig. 10 shows the oxidation degradation mechanism of the urchin-like SiO_2@MnO_2 particles to RhB. Initially, due to the special urchin-like structure, which provides strong capillary force and more oxidation active sites, RhB molecules are fast adsorbed and enriched in the pores of the urchin-like SiO_2@γ-MnO_2 microparticles, and subsequently degraded by MnO_2. In the degradation process, the color of the dye solution changed from pink to light yellow green, and finally to colorless. In the corresponding UV spectra, the blue shift of the absorption peak to about 493 nm can be attributed to the *n*-deethylation of RhB.[48] The further decolorization of the solution indicates the destruction of the conjugated xanthene structure

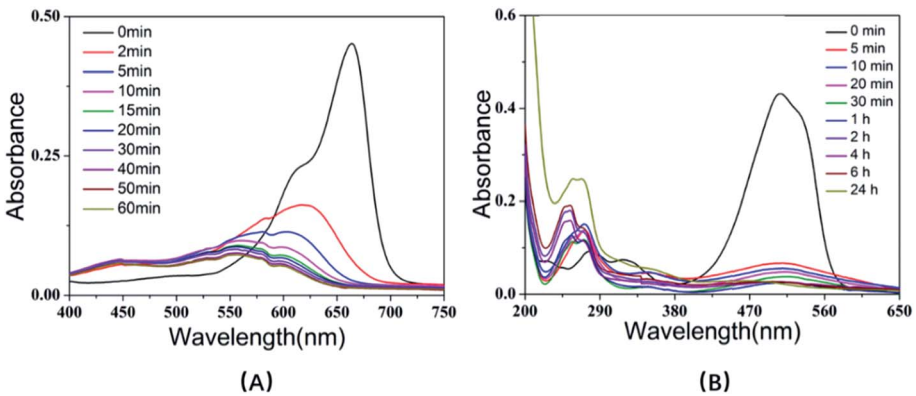

Fig. 8 UV-Vis spectra of methylene blue (A) and methyl orange (B) solution with urchin-like hollow SiO_2@γ-MnO_2 microparticles at pH = 3.5.

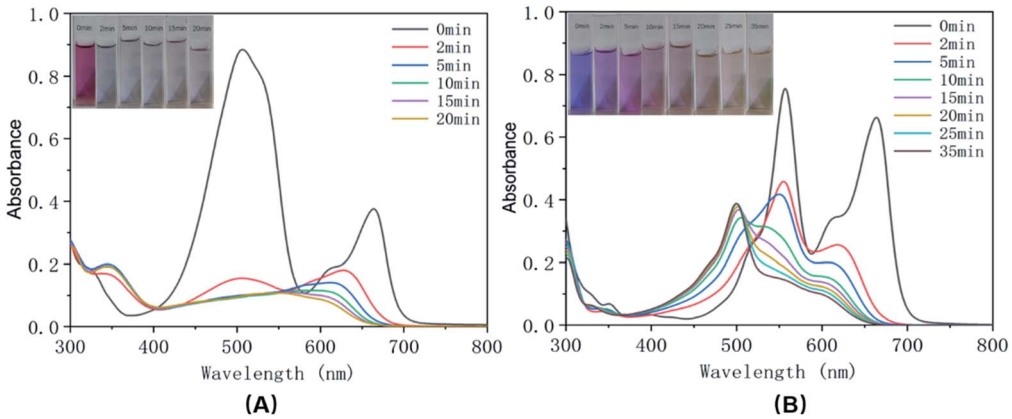

Fig. 9 UV-Vis spectra of the mixed solution of methyl orange and methylene blue (A) and the mixed solution of RhB and methylene blue (B) with the urchin-like hollow SiO_2@γ-MnO_2 microparticles at pH = 3.5.

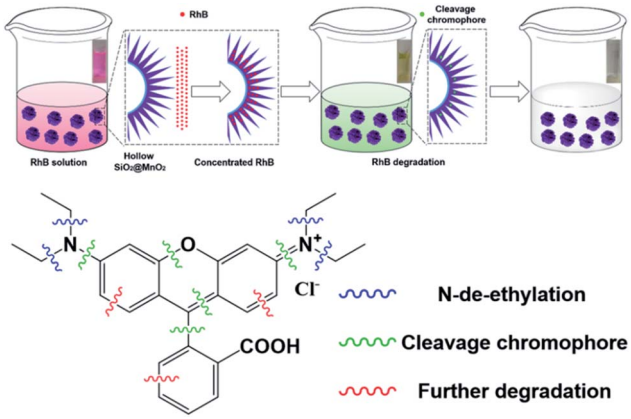

Fig. 10 The oxidative degradation of RhB by the urchin-like SiO_2@γ-MnO_2 microparticles.

(chromophore).[49,50] On the other hand. Because of the continuous degradation of RhB by MnO_2, the concentration of RhB in the micropores of the urchin-like SiO_2@γ-MnO_2 microparticles is low, and the continuous diffusion and transfer of RhB to surface of the MnO_2 microparticles is driven by the concentration difference of RhB.

Fig. 11 show that after five cycles of continuous use of the sea urchin-like hollow SiO_2@MnO_2 microparticles, the degradation rate of RhB still reached 82%, which indicates that the urchin-like hollow SiO_2@MnO_2 microparticles have good reuse efficiency.

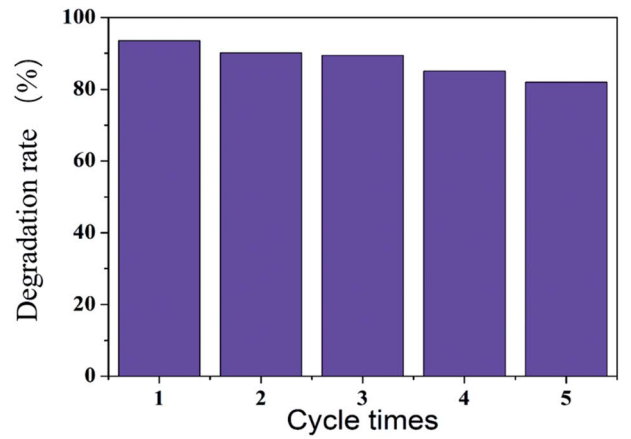

Fig. 11 Degradation rate of rhodamine B by the continuous use of urchin-like SiO_2@γ-MnO_2 microparticles.

4. Conclusion

In this paper, using hollow SiO_2 microspheres as the template, urchin-like SiO_2@γ-MnO_2 microparticles were synthesized by facile oxidation-reduction precipitation method at room temperature. This method overcomes some shortcomings of traditional hydrothermal method such as high temperature requirement and low coating amount. Furthermore, in acidic solution, the as-prepared microparticles showed high oxidative degradation efficiency for organic dyes in a short time (RhB 87.1% and methyl orange 87.5% in 10 min). In addition, it still showed good degradation performance for the mixed dye solution. This research shows broad application prospects for solving some important environmental problems in the related industry.

Conflicts of interest

There are no conflicts to declare.

Acknowledgements

This work was partly supported by "Research and Development (R&D) Plan of Jurong City" (ZY2019006, Jiangsu Province, China).

Notes and references

1 P. Moradihamedani, Recent advances in dye removal from wastewater by membrane technology: a review, *Polym. Bull.*, 2021, 1–29.

2 K. Guo, B. Gao, J. Wang, J. Pan, Q. Yue and X. Xu, Flocculation behaviors of a novel papermaking sludge-based flocculant in practical printing and dyeing wastewater treatment, *Front. Environ. Sci. Eng.*, 2021, **15**, 103.
3 L. Meng, M. Wu, H. Chen, Y. Xi, M. Huang and X. Luo, Rejection of antimony in dyeing and printing wastewater by forward osmosis, *Sci. Total Environ.*, 2020, **745**, 141015.
4 X. Wei, S. Cao, J. Hu, Y. Chen, R. Yang, J. Huang, Z. Wang, Q. Zhou and J. Chen, Graphene oxide/multi-walled carbon nanotubes nanocompsite polyamide nanofiltration membrane for dyeing-printing wastewater treatment, *Polym. Adv. Technol.*, 2021, **32**, 690–702.
5 Y. Junejo, Sirajuddin, A. Baykal, M. Safdar and A. Balouch, A novel green synthesis and characterization of Ag NPs with its ultra-rapid catalytic reduction of methyl green dye, *Appl. Surf. Sci.*, 2014, **290**, 499–503.
6 R. Mallampati, L. Xuanjun, A. Adin and S. Valiyaveettil, Fruit Peels as Efficient Renewable Adsorbents for Removal of Dissolved Heavy Metals and Dyes from Water, *ACS Sustainable Chem. Eng.*, 2015, **3**, 1117–1124.
7 H. Zhou, L. Zhou and K. Ma, Microfiber from textile dyeing and printing wastewater of a typical industrial park in China: Occurrence, removal and release, *Sci. Total Environ.*, 2020, **739**, 140329.
8 J. Liang, X.-A. Ning, J. Sun, J. Song, Y. Hong and H. Cai, An integrated permanganate and ozone process for the treatment of textile dyeing wastewater: Efficiency and mechanism, *J. Cleaner Prod.*, 2018, **204**, 12–19.
9 G. T. Güyer, K. Nadeem and N. Dizge, Recycling of pad-batch washing textile wastewater through advanced oxidation processes and its reusability assessment for Turkish textile industry, *J. Cleaner Prod.*, 2016, **139**, 488–494.
10 A. G. Khorram and N. Fallah, Treatment of textile dyeing factory wastewater by electrocoagulation with low sludge settling time: Optimization of operating parameters by RSM, *J. Environ. Chem. Eng.*, 2018, **6**, 635–642.
11 A. Mukimin, N. Zen, A. Purwanto, K. A. Wicaksono, H. Vistanty and A. S. Alfauzi, Application of a full-scale electrocatalytic reactor as real batik printing wastewater treatment by indirect oxidation process, *J. Environ. Chem. Eng.*, 2017, **5**, 5222–5232.
12 J. Wang, T. Zhang, Y. Mei and B. Pan, Treatment of reverse-osmosis concentrate of printing and dyeing wastewater by electro-oxidation process with controlled oxidation-reduction potential (ORP), *Chemosphere*, 2018, **201**, 621–626.
13 P. Hu, H. Su, Z. Chen, C. Yu, Q. Li, B. Zhou, P. J. J. Alvarez and M. Long, Selective Degradation of Organic Pollutants Using an Efficient Metal-Free Catalyst Derived from Carbonized Polypyrrole *via* Peroxymonosulfate Activation, *Environ. Sci. Technol.*, 2017, **51**, 11288–11296.
14 S. Peng, X. Yang, J. Strong, B. Sarkar, Q. Jiang, F. Peng, D. Liu and H. Wang, MnO_2-decorated N-doped carbon nanotube with boosted activity for low-temperature oxidation of formaldehyde, *J. Hazard. Mater.*, 2020, **396**, 122750.
15 A.-Y. Zhang, P.-C. Zhao, Y.-Y. He, Y. Zhou and J.-W. Feng, Non-radical activation of H_2O_2 by surface-disordered WO3 for efficient and selective pollutant degradation with weak matrix effects, *Environ. Sci. Pollut. Res.*, 2020, **27**, 1898–1911.
16 M. L. Chacón-Patiño, C. Blanco-Tirado, J. P. Hinestroza and M. Y. Combariza, Biocomposite of nanostructured MnO_2 and fique fibers for efficient dye degradation, *Green Chem.*, 2013, **15**, 2920–2928.
17 Y. Liu, R. Qu, X. Li, Y. Wei and L. Feng, A bifunctional b-MnO2 mesh for expeditious and ambient degradation of dyes in activation of peroxymonosulfate (PMS) and simultaneous oil removal from water, *J. Colloid Interface Sci.*, 2020, **579**, 412–424.
18 W. Qian, H. Huang, Z. Diao, H. Li, H. Liu, M. Ye, Y. Deng and Z. Xu, Advanced treatment of dye wastewater using a novel integrative Fenton-like/MnO2-filled upward flow biological filter bed system equipped with modified ceramsite, *Environ. Res.*, 2021, **194**, 110641.
19 R. Yang, Y. Fan, R. Ye, Y. Tang, X. Cao, Z. Yin and Z. Zeng, MnO2-Based Materials for Environmental Applications, Advanced, *Material*, 2021, **33**, 2004862.
20 J. Han, M. Wang, S. Cao, P. Fang, S. Lu, R. Chen and R. Guo, Reactive template strategy for fabrication of MnO_2/polyaniline coaxial nanocables and their catalytic application in the oxidative decolorization of rhodamine B, *J. Mater. Chem. A*, 2013, **1**, 13197–13202.
21 M. He, L. Cao, W. Li, X. Chang and Z. Ren, α-MnO_2 nanotube@δ-MnO_2 nanoflake hierarchical structure on three-dimensional graphene foam as a lightweight and free-standing supercapacitor electrode, *J. Alloys Compd.*, 2021, **865**, 158934.
22 S. Subhan, M. Yaseen, B. Ahmad, Z. Tong, F. Subhan, W. Ahmad and M. Sahibzada, Fabrication of MnO2 NPs incorporated UiO-66 for the green and efficient oxidative desulfurization and denitrogenation of fuel oils, *J. Environ. Chem. Eng.*, 2021, **9**, 105179.
23 L. Zhang, X. Liu, L. Luo, C. Hu, J. Fu, X. Chang and T. Gan, A high-performance voltammetric methodology for the ultra-sensitive detection of riboflavin in food matrices based on graphene oxide-covered hollow MnO2 spheres, *Food Chem.*, 2021, **352**, 129368.
24 Z. I. Abbas and A. S. Abbas, Oxidative degradation of phenolic wastewater by electro-fenton process using MnO_2-graphite electrode, *J. Environ. Chem. Eng.*, 2019, **7**, 103108.
25 J. Li, B. Hu, P. Nie, X. Shang, W. Jiang, K. Xu, J. Yang and J. Liu, Fe-regulated δ-MnO_2 nanosheet assembly on carbon nanofiber under acidic condition for high performance supercapacitor and capacitive deionization, *Appl. Surf. Sci.*, 2021, **542**, 148715.
26 T. Tian, S. Qiao, C. Yu and J. Zhou, Effects of nano-sized MnO_2 on methanogenic propionate and butyrate degradation in anaerobic digestion, *J. Hazard. Mater.*, 2019, **364**, 11–18.
27 Z. Wang, H. Jia, Z. Liu, Z. Peng, Y. Dai, C. Zhang, X. Guo, T. Wang and L. Zhu, Greatly enhanced oxidative activity of δ-MnO_2 to degrade organic pollutants driven by dominantly exposed {−111} facets, *J. Hazard. Mater.*, 2021, **413**, 125285.

28 L. Xu, J. Fang, Y. Tan, J. Xu, H. Tang, Z. Han, M. Zhang, T. Yu, H. Jin, H. Ge, X. Wang, D. Jin and H. Lou, Facile preparation of high performance degradation of HCHO catalyst from Li-MnO2 batteries, *Mater. Lett.*, 2020, **260**, 126958.

29 Y. Yamaguchi, R. Aono, E. Hayashi, K. Kamata and M. Hara, Template-Free Synthesis of Mesoporous β-MnO2 Nanoparticles: Structure, Formation Mechanism, and Catalytic Properties, *ACS Appl. Mater. Interfaces*, 2020, **12**, 36004–36013.

30 M. Zhang, H. Zheng, H. Zhu, Z. Xu, R. Liu, J. Chen, Q. Song, X. Song, J. Wu, C. Zhang and H. Cui, Graphene-wrapped MnO_2 achieved by ultrasonic-assisted synthesis applicable for hybrid high-energy supercapacitors, *Vacuum*, 2020, **176**, 109315.

31 S. Park, H.-W. Shim, C. W. Lee, H. J. Song, I. J. Park, J.-C. Kim, K. S. Hong and D.-W. Kim, Tailoring uniform γ-MnO_2 nanosheets on highly conductive three-dimensional current collectors for high-performance supercapacitor electrodes, *Nano Res.*, 2015, **8**, 990–1004.

32 Y. Cheng, X. Wu, L. Xu, Z. Jiang, C. Liu, Q. Zhang, Y. Zou, Y. Chen, J. Li and X. Liu, Magnetically separable and recyclable ternary photocatalyst MnxZn1-xFe_2O_4/$BiVO_4$/MnO_2 with excellent photocatalytic activity, *Vacuum*, 2021, **187**, 110133.

33 T. L. B. Ferreira, L. M. P. Garcia, G. H. M. Gurgel, R. M. Nascimento, M. J. Godinho, M. H. M. Rodrigues, M. R. D. Bomio and F. V. Motta, Effects of MnO_2/In_2O_3 thin films on photocatalytic degradation 17 alpha-ethynylestradiol and methylene blue in water, *J. Mater. Sci.: Mater. Electron.*, 2018, **29**, 12278–12287.

34 P. C. Metz, A. C. Ladonis, P. Gao, T. Hey and S. T. Misture, Hierarchical porosity *via* layer-tunnel conversion of macroporous δ-MnO2 nanosheet assemblies, *RSC Adv.*, 2020, **10**, 1484–1497.

35 S. I. Siddiqui, O. Manzoor, M. Mohsin and S. A. Chaudhry, Nigella sativa seed based nanocomposite-MnO_2/BC: An antibacterial material for photocatalytic degradation, and adsorptive removal of Methylene blue from water, *Environ. Res.*, 2019, **171**, 328–340.

36 L. Song, C. Li, W. Chen, B. Liu and Y. Zhao, Highly efficient MnO_2/reduced graphene oxide hydrogel motors for organic pollutants removal, *J. Mater. Sci.*, 2020, **55**, 1984–1995.

37 H. R. Barai, M. M. Rahman, A. Rahim and S. W. Joo, α-MnO_2 nanorod/boron nitride nanoplatelet composites for high-performance nanoscale dielectric pseudocapacitor applications, *J. Ind. Eng. Chem.*, 2019, **79**, 115–123.

38 W. Zong, Z. Guo, M. Wu, X. Yi, H. Zhou, S. Jing, J. Zhan, L. Liu and Y. Liu, Synergistic multiple active species driven fast estrone oxidation by δ-MnO_2 in the existence of methanol, *Sci. Total Environ.*, 2021, **761**, 143201.

39 S. Ghosal and P. Bhattacharyya, Time Dependent Morphological Evolution of Hydrothermally Derived MnO_2 Nanostructures and Corresponding Methanol Vapor Sensing Performance, *IEEE Trans. Nanotechnol.*, 2019, **18**, 502–508.

40 D.-S. Liu, Y. Mai, S. Chen, S. Liu, E. H. Ang, M. Ye, Y. Yang, Y. Zhang, H. Geng and C. C. Li, A 1D–3D interconnected δ-MnO_2 nanowires network as high-performance and high energy efficiency cathode material for aqueous zinc-ion batteries, *Electrochim. Acta*, 2021, **370**, 137740.

41 B. Sharma, A. A. Kadam, J.-S. Sung and J.-h. Myung, Surface tuning of halloysite nanotubes with Fe3O4 and 3-D MnO_2 nanoflakes for highly selective and sensitive acetone gas sensing, *Ceram. Int.*, 2020, **46**, 21292–21303.

42 H. Shen, X. Kong, P. Zhang, X. Song, H. Wang and Y. Zhang, In-situ hydrothermal synthesis of δ-MnO_2/soybean pod carbon and its high performance application on supercapacitor, *J. Alloys Compd.*, 2021, **853**, 157357.

43 G. Zhu, J. Gen, L. Yan, Y. K. Yuan and G. Z. Han, Homogeneous magnetic Ag-Au alloy microparticles for ultrasensitive catalytic reduction of aromatic nitro compounds, *Colloids Surf., A*, 2019, **580**, 123697.

44 X. Fu, J. Feng, H. Wang and K. M. Ng, Morphological and structural evolution of α-MnO_2 nanorods synthesized *via* an aqueous route through MnO_4^-/Mn^{2+} reaction, *J. Solid State Chem.*, 2010, **183**, 883–889.

45 L. Cheng, Y. Liu, B. Zou, Y. Yu, W. Ruan and Y. Wang, Template-etching route to construct uniform rattle-type Fe_3O_4@SiO_2 hollow microspheres as drug carrier, *Mater. Sci. Eng., C*, 2017, **75**, 829–835.

46 M. Wang, H. Liu, Z.-H. Huang and F. Kang, Activated carbon fibers loaded with MnO_2 for removing NO at room temperature, *Chem. Eng. J.*, 2014, **256**, 101–106.

47 G. Zhao, J. Li, X. Ren, J. Hu, W. Hu and X. Wang, Highly active MnO_2 nanosheet synthesis from graphene oxide templates and their application in efficient oxidative degradation of methylene blue, *RSC Adv.*, 2013, **3**, 12909–12914.

48 Y. Xie, L. Lv, S. Zhang, B. Pan, X. Wang, Q. Chen, W. Zhang and Q. Zhang, Fabrication of anion exchanger resin/nano-CdS composite photocatalyst for visible light RhB degradation, *Nanotechnology*, 2011, **22**, 305707.

49 K. Yu, S. Yang, H. He, C. Sun, C. Gu and Y. Ju, Visible Light-Driven Photocatalytic Degradation of Rhodamine B over $NaBiO_3$: Pathways and Mechanism, *J. Phys. Chem. A*, 2009, **113**, 10024–10032.

50 H. Fu, S. Zhang, T. Xu, Y. Zhu and J. Chen, Photocatalytic Degradation of RhB by Fluorinated Bi_2WO_6 and Distributions of the Intermediate Products, *Environ. Sci. Technol.*, 2008, **42**, 2085–2091.